# Electromagnetic Scattering by Networks of High-Permittivity Thin Wires

Carlo Forestiere,[1,*] Giovanni Miano,[1] and Bruno Miranda[1,2]

[1] *Department of Electrical Engineering and Information Technology, Università degli Studi di Napoli Federico II, via Claudio 21, Napoli 80125, Italy*

[2] *Institute of Applied Sciences and Intelligent Systems – Unit of Naples, National Research Council, via P. Castellino 111, Naples 80131, Italy*

(Received 9 February 2021; revised 6 May 2021; accepted 3 June 2021; published 7 July 2021)

The electromagnetic scattering from a network of high-permittivity dielectric thin wires with the network's size smaller than or almost equal to the operating wavelength is investigated. A simple lumped-element theory for the polarization current intensities induced in the wires is developed. The network elements are capacitances and inductances between the wires. An analytical expression for the induced polarization currents is obtained. The connection between the spectral properties of the loop inductance matrix and the network's resonances is established. The number of the allowed current modes and resonances is deduced from the topology of the circuit's digraph. The radiative coupling is also included, and the radiative frequency shifts and the quality factors are derived. The introduced concept and methods may find applications both at radio frequencies and in nanophotonics.

DOI: 10.1103/PhysRevApplied.16.014015

## I. INTRODUCTION

High-permittivity dielectric objects [1] are currently intensively studied both at radio frequencies and in the visible, promising diverse applications including dielectric resonator antennas [2], nanoscale biosensors [3], wireless midrange energy transfer [4], nonlinear optics [5], and metamaterials [6]. At radio frequencies, materials with very high refractive index are routinely fabricated [7,8], and there is currently a great interest in their additive manufacturing [9]. In the visible and infrared ranges, scientists are constantly searching for better materials with higher refractive indices, developing innovative fabrication methods and improving the existing ones [10].

Among the many types of high-permittivity structures, thin wires constitute a promising building block of all-dielectric metamaterials and may play a role as important as that played in the last decades by *conducting* thin wires [11,12]. For instance, at optical frequencies, periodic arrangements of high-permittivity nanowires have been proposed [13,14] as magnetic media, while at microwaves, a dielectric resonator antenna, obtained by a convenient arrangement of high-permittivity wires, has recently been designed and fabricated [15]. The analysis and design of electromagnetic scattering from high-permittivity thin-wire structures may benefit from simple models able to describe their main physical properties with a reduced computational cost.

In this paper, we propose a lumped-element theory to describe the electromagnetic scattering from networks of high-permittivity thin wires, denoted as *dielectric networks*. This theory is developed in the framework of the magnetoquasistatic approximation of the Maxwell equations [16,17] with radiative corrections [18]. This approximation adequately describes the electromagnetic scattering by high-permittivity structures with size smaller than or at almost equal to the operating wavelength. The induced polarization density field is solenoidal and its normal component to the surface of the objects is equal to zero [19]. Therefore, high-permittivity wires behave as flux tubes for the polarization current, playing an analogous role to high conductive wires in traditional electric networks.

The lumped-element theory is based on the concepts of capacitances, self- and mutual inductances between the wires, and on the graph theory. It leads to the analytical prediction of the polarization currents induced in the dielectric network by an external electromagnetic field; the current modes and the resonance frequencies, their radiative shifts, and quality factors. Specifically, we find that the spectral properties of the loop inductance matrix of the dielectric network determine its electromagnetic scattering resonances and modes. Thus, instead of solving Maxwell's equation, which would be unpractical for intricate connections of multiple branches, we import concepts and formulas that have been developed by scientists and engineers working on electric networks [20], in particular the analytic formulas produced in the first twenty years of the twentieth century and summarized in the manuscripts

---

[*] carlo.forestiere@unina.it

of Rosa [21], Grover [22], and Weber [23]. These concepts are now applied to the polarization current densities, rather than to the conduction currents, consistently with the framework proposed by Engheta and coworkers in Refs. [24–27]. In particular, one of the main strengths of the proposed model lies in its simplicity: when the network consists of only a few loops, the calculation of the resonance current modes and the associated frequencies can be carried out with just paper and pencil, together with their radiative frequency shifts and quality factors. It also enucleates the connection between the current modes, resonances, radiative corrections, and the topology of the underlying graph.

The paper is organized as follows. After a brief summary of the properties of the magnetoquasistatic current modes, resonances, and radiative corrections, we introduce—through examples of increasing complexity—the steps required to assemble a lumped-element model for complex high-permittivity dielectric networks. First, in Sec. III we consider an isolated high-permittivity loop, and we link its self-inductance with the resonance frequency and the radiative quality factor. Then, in Sec. IV, we extend the lumped-element model to two interacting high-permittivity loops. Eventually, we consider in Sec. V an arbitrary interconnection of high-permittivity thin wires.

## II. ELECTROMAGNETIC SCATTERING FROM A HIGH-PERMITTIVITY DIELECTRIC OBJECT

In the linear regime, resonant electromagnetic scattering from nonmagnetic and small objects occurs according to two different mechanisms (see, e.g., Refs. [17,18]). If the real part of the permittivity is negative (e.g., as in metals), resonances arise from the interplay between the electric field energy of the electroquasistatic current modes and the polarization energy. Instead, if the real part of the permittivity is positive and very high (e.g., as in dielectrics), resonances arise from the interplay between the magnetic field energy of the magnetoquasistatic current modes and the polarization energy. The quasistatic current density modes are solutions of the source-free Maxwell equations in the quasistatic limits. In particular, the magnetoquasistatic current density modes are solenoidal in the object and their normal component to the boundary of the object is equal to zero. In the following, we briefly resume the principal features of the magnetoquasistatic current density modes together with their radiative corrections (for details, see Refs. [17,18]).

Let us consider an isotropic and homogeneous dielectric surrounded by vacuum and occupying a volume $\Omega$; $\partial\Omega$ is the boundary of $\Omega$ with outward-pointing normal $\hat{\mathbf{n}}$. The object is illuminated by a time harmonic electromagnetic field incoming from infinity $\mathrm{Re}\{\mathbf{E}_{\mathrm{ext}}(\mathbf{r})e^{i\omega t}\}$, where $\omega$ is the angular frequency. We denote with $\varepsilon_R$ the relative permittivity of the object, with $\chi = \varepsilon_R - 1$ the susceptibility, and with $\varepsilon_0$ the vacuum permittivity. We introduce the dimensionless size parameter of the object $x = \omega/\omega_c$, where $\omega_c = c_0/l_c$, $l_c$ is a characteristic dimension of the dielectric object, and $c_0$ is the light velocity in vacuum; $x$ is equal to the ratio between $l_c$ and the operating wavelength in vacuum.

### A. Magnetoquasistatic approximation

In dielectric objects with high relative permittivity, $\epsilon_R \gg 1$, and with sizes much smaller than the operating wavelength, $x \ll 1$, the induced polarization current density field is given by [17,18]

$$\mathbf{J}(\tilde{\mathbf{r}}) = i\omega\chi\varepsilon_0 \sum_h \frac{1}{1 - x^2\chi/\kappa_h^{\perp}} \langle \mathbf{j}_h, \mathbf{E}_{\mathrm{ext}}\rangle\, \mathbf{j}_h(\tilde{\mathbf{r}}), \qquad (1)$$

where the magnetoquasistatic current density modes $\{\mathbf{j}_h(\tilde{\mathbf{r}})\}$ are solutions of the eigenvalue problem [17]

$$\frac{1}{4\pi}\int_{\tilde{\Omega}} \frac{\mathbf{j}_h(\tilde{\mathbf{r}}')}{|\tilde{\mathbf{r}} - \tilde{\mathbf{r}}'|}\, d\tilde{V}' = \frac{1}{\kappa_h^{\perp}}\mathbf{j}_h(\tilde{\mathbf{r}}) \quad \text{for all } \tilde{\mathbf{r}} \in \tilde{\Omega} \qquad (2)$$

with

$$\mathbf{j}_h(\tilde{\mathbf{r}}) \cdot \hat{\mathbf{n}}(\tilde{\mathbf{r}}) = 0 \quad \text{for all } \tilde{\mathbf{r}} \in \partial\tilde{\Omega}, \qquad (3)$$

and $\kappa_h^{\perp}$ is the eigenvalue associated with the eigenfunction $\mathbf{j}_h(\tilde{\mathbf{r}})$; $\langle \mathbf{A}, \mathbf{B}\rangle = \int_{\tilde{\Omega}} \mathbf{A}\cdot\mathbf{B}\, dV$ is the standard inner product. In Eqs. (1)–(3) the position vector $\mathbf{r}$ has been normalized by $l_c$, i.e., $\tilde{\mathbf{r}} = \mathbf{r}/l_c$, and $\tilde{\Omega}$ is the corresponding scaled domain and $\partial\tilde{\Omega}$ its boundary.

Apart from the factor $\mu_0$, the integral operator on the left-hand side of Eq. (2) gives the static magnetic vector potential in the Coulomb gauge as a function of the current density field (here we call it the magnetoquasistatic integral operator). Equation (2) holds in weak form in the functional space equipped with the inner product $\langle \mathbf{A}, \mathbf{B}\rangle$, and constituted by the vector fields that are solenoidal in $\tilde{\Omega}$ and have zero normal component to $\partial\tilde{\Omega}$. The spectrum of the magnetoquasistatic integral operator is discrete $\{\kappa_h^{\perp}\}_{h\in\mathbb{N}}$, and the eigenvalues are real and positive [17]. The current density modes $\{\mathbf{j}_h\}_{h\in\mathbb{N}}$ are solenoidal in $\tilde{\Omega}$, have zero normal component to $\partial\tilde{\Omega}$, and are orthonormal according to the scalar product $\langle \mathbf{A}, \mathbf{B}\rangle$. The modes are ordered in such a way that $\kappa_0^{\perp} < \kappa_1^{\perp} < \kappa_2^{\perp} < \cdots$. Equation (1) has been obtained by solving the full-wave electromagnetic scattering problem in the quasistatic limit (for details, see Refs. [17,18]). In Eq. (1) we have disregarded the contribution of the electroquasistatic current density modes because they give nonresonant terms in the electromagnetic scattering from a high-index dielectric.

The resonance frequency $\omega_h$ of the $h$th mode $\mathbf{j}_h$ is obtained by maximizing its amplitude in Eq. (1). It is the solution of the equation [17,18]

$$\left(\frac{\omega_h}{\omega_c}\right)^2 \mathrm{Re}\{\chi(\omega_h)\} = \kappa_h^{\perp}. \tag{4}$$

If the material is nondispersive, the normalized resonance frequency is equal to the square root of the ratio between the magnetoquasistatic eigenvalue and the susceptibility. Equation (4) highlights that the resonance arises from the interplay between the energy stored in the magnetic field (proportional to $1/\kappa_h^{\perp}$) and the polarization energy of the dielectric (proportional to the real part of $\chi$).

### B. Radiative corrections

When the dimensionless size parameter of the object becomes almost equal to one, $x \simeq 1$, the set of modes $\{\mathbf{j}_h\}$ still approximates well the modes of the objects; nevertheless, the magnetoquasistatic approximation cannot provide their radiative shift and quality factors. The results obtained by the magnetoquasistatic approximation have to be supplemented by radiative corrections [18]. Indeed, Eq. (1) is still a valid approximation for the induced polarization current density when $x \simeq 1$ as long as $\kappa_h^{\perp}$ is replaced with

$$\kappa_h = \kappa_h^{\perp} + \kappa_h^{(1)} x + \kappa_h^{(2)} x^2 + \cdots + \kappa_h^{(n_i)} x^{n_i} + \cdots, \tag{5}$$

where $\kappa_h^{(n)}$ is the $n$th coefficient in the expansion of $\kappa_h$ in a power series of $x$ (for details, see Ref. [18]). For any object's shape, $\kappa_h^{(1)} = 0$ and $\kappa_h^{(2)}$ is real. Taking into account the second-order correction $\kappa_h^{(2)}$, we find that the resonance frequency is the solution of the equation

$$[\mathrm{Re}\{\chi(\omega_h)\} - \kappa_h^{(2)}]\left(\frac{\omega_h}{\omega_c}\right)^2 = \kappa_h^{\perp}. \tag{6}$$

The coefficient $\kappa_h^{(2)}$ is negative; therefore, the second-order radiative correction introduces a negative frequency shift with respect to the quasistatic resonance given by Eq. (4). The first nonvanishing imaginary correction $\kappa_h^{(n_i)}$ has order $n_i \geq 3$, and has a positive imaginary part. It determines the radiative broadening of the mode, related to the inverse of the quality factor, which is given by [18]

$$Q_h = \left|\frac{\kappa_h^{\perp}}{\kappa_h^{(n_i)}}\right| \left(\frac{1}{x_h}\right)^{n_i}, \tag{7}$$

where $x_h$ is the size parameter evaluated at the resonance frequency given by Eq. (6). The order of the first nonvanishing imaginary correction $n_i$ returns the multipolar scattering order [18]. For instance, the modes with $n_i = 3$ exhibit a nonvanishing magnetic dipole moment, and those with $n_i = 5$ have zero magnetic dipole moment but either nonzero magnetic quadrupole or nonzero $P_{E2}$ moment [28] (also called the toroidal dipole), etc. The general expressions for the radiation corrections of magnetoquasistatic current density modes are given in Ref. [18].

## III. ISOLATED HIGH-PERMITTIVITY THIN-WIRE LOOP

We now consider a dielectric loop made of a high-permittivity thin wire with uniform cross section $\Sigma$ (the transverse linear dimensions are much smaller compared to the length). The wire axis is represented by the closed curve $\Gamma$ with tangent unit vector $\hat{\mathbf{t}}$. With abuse of notation, we also indicate with $\Sigma$ the cross-sectional area, with $\Gamma$ the loop length, and with $\Omega$ the loop volume, which is given by $\Omega = \Gamma \times \Sigma$.

### A. Fundamental magnetoquasistatic current mode

In a loop with small cross section, the lowest eigenvalue $\kappa_0^{\perp}$ is well separated from the remaining eigenvalues, as shown in Ref. [17] for a loop of finite cross section. This separation increases as the wire cross section reduces. This fact suggests that, for $x$ smaller than or almost comparable to one in a thin-wire dielectric loop, only the mode $\mathbf{j}_0(\tilde{\mathbf{r}})$ associated with the smallest eigenvalue $\kappa_0^{\perp}$ (fundamental magnetoquasistatic mode) is excited. Therefore, in this case the expression of the induced polarization current density (1) reduces to

$$\mathbf{J}(\tilde{\mathbf{r}}) = i\omega\chi\varepsilon_0 \frac{1}{1 - x^2\chi/\kappa_0^{\perp}} \langle \mathbf{j}_0, \mathbf{E}_{\mathrm{ext}} \rangle \mathbf{j}_0(\tilde{\mathbf{r}}). \tag{8}$$

The fundamental mode $\mathbf{j}_0(\tilde{\mathbf{r}})$ is directed along the wire axis $\hat{\mathbf{t}}$, and its module is uniform along the axis, and almost uniform in the cross section (as shown in Ref. [17] for a loop of finite cross section),

$$\mathbf{j}_0(\tilde{\mathbf{r}}) = \begin{cases} \hat{\mathbf{t}}(\tilde{\mathbf{r}})/\sqrt{\tilde{\Omega}} & \text{in } \tilde{\Omega}, \\ \mathbf{0} & \text{otherwise.} \end{cases} \tag{9}$$

The mode is normalized in such a way that $\langle \mathbf{j}_0, \mathbf{j}_0 \rangle = 1$. The corresponding eigenvalue $\kappa_0^{\perp}$ is given by Eq. (2), i.e.,

$$\frac{\tilde{\Omega}}{\kappa_0^{\perp}} = \frac{1}{4\pi} \int_{\tilde{\Omega}} \int_{\tilde{\Omega}} \frac{\hat{\mathbf{t}}(\tilde{\mathbf{r}}) \cdot \hat{\mathbf{t}}(\tilde{\mathbf{r}}')}{|\tilde{\mathbf{r}} - \tilde{\mathbf{r}}'|} d\tilde{V}' \, d\tilde{V}, \tag{10}$$

where $\tilde{\Omega}$ on the left-hand side denotes the scaled volume of the object ($\tilde{\Omega} = \Gamma \times \Sigma / l_c^3$). Apart from the factor $(l_c^5/\Sigma^2)\mu_0$, the integral of the right-hand side is equal to the self-inductance of the loop $L$; therefore,

$$\kappa_0^{\perp} = \frac{l_c \Gamma}{\Sigma} \frac{l_c \mu_0}{L}. \tag{11}$$

### B. Lumped-element model for a single loop

Equation (8) has a very simple physical explanation. The polarization current density field induced in the loop is given by

$$\mathbf{J} = i\omega\varepsilon_0\chi(\mathbf{E}+\mathbf{E}_{\text{ext}}), \tag{12}$$

where $\mathbf{E}$ is the induced electric field. By performing the line integral along $\Gamma$ on both sides of Eq. (12) we obtain

$$\frac{1}{\chi}\frac{1}{i\omega C}I = \mathcal{E}_{\text{ext}} + \mathcal{E}, \tag{13}$$

where $I$ is the intensity of the induced polarization current in the wire,

$$C = \varepsilon_0\frac{\Sigma}{\Gamma}, \tag{14}$$

$\mathcal{E}$ is the induced voltage along the loop,

$$\mathcal{E} = \oint_\Gamma \mathbf{E}\cdot\hat{\mathbf{t}}\,dl, \tag{15}$$

and $\mathcal{E}_{\text{ext}}$ is the applied voltage,

$$\mathcal{E}_{\text{ext}} = \oint_\Gamma \mathbf{E}_{\text{ext}}\cdot\hat{\mathbf{t}}\,dl. \tag{16}$$

On the other hand, from the Faraday law we obtain

$$\mathcal{E} = -i\omega LI, \tag{17}$$

where $L$ is the self-inductance of the loop. Substituting Eq. (17) into Eq. (13) we have

$$\left(i\omega L + \frac{1}{\chi}\frac{1}{i\omega C}\right)I = \mathcal{E}_{\text{ext}}, \tag{18}$$

which is the equation governing the equivalent circuit in Fig. 1. Since, from Eqs. (11) and (14),

$$\frac{1}{\omega_c^2\kappa_0^\perp} = LC, \tag{19}$$

the solution of Eq. (18) is expressed as

$$I = i\omega C\chi\frac{1}{1-(\omega/\omega_c)^2\chi/\kappa_0^\perp}\mathcal{E}_{\text{ext}}. \tag{20}$$

This expression coincides with the expression of the polarization current intensity obtained from Eq. (8).

The quasistatic resonance frequency, the solution of Eq. (4), is the value of $\omega$ for which $|1-(\omega/\omega_c)^2\chi/\kappa_0^\perp|$ is minimum.

The developed model can be applied, without any modification, to complex susceptibilities. In particular, when the $\chi$ becomes complex, the capacitance $\chi C$ in Fig. 1 becomes complex as well. Thus, the corresponding impedance exhibits a nonzero real part, namely a resistance.

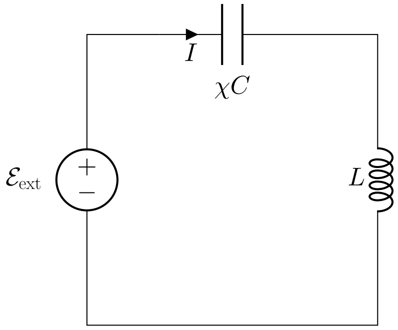

FIG. 1. Lumped-element circuit for a high-permittivity loop.

### C. Radiative corrections

In the case of the considered dielectric loop the radiative corrections $\kappa_h^{(2)}$ and $\kappa_h^{(3)}$ have the following forms [18]:

$$\kappa_0^{(2)} = \frac{(\kappa_0^\perp)^2}{8\pi}\int_{\tilde\Omega}\int_{\tilde\Omega}|\tilde{\mathbf{r}}-\tilde{\mathbf{r}}'|\,\mathbf{j}_0(\tilde{\mathbf{r}})\cdot\mathbf{j}_0(\tilde{\mathbf{r}}')\,d\tilde V'\,d\tilde V, \tag{21}$$

$$\kappa_0^{(3)} = -i\frac{(\kappa_0^\perp)^2}{24\pi}\int_{\tilde\Omega}\int_{\tilde\Omega}|\tilde{\mathbf{r}}-\tilde{\mathbf{r}}'|^2\,\mathbf{j}_0(\tilde{\mathbf{r}})\cdot\mathbf{j}_0(\tilde{\mathbf{r}}')\,d\tilde V'\,d\tilde V. \tag{22}$$

Using Eq. (9), Eq. (21) becomes

$$\kappa_0^{(2)} = -2\pi\frac{\Sigma}{\Gamma^2}(\kappa_0^\perp)^2\Delta, \tag{23}$$

where

$$\Delta = -\frac{1}{8\pi}\oint_{\tilde\Gamma}\oint_{\tilde\Gamma}\hat{\mathbf{t}}(\tilde{\mathbf{r}})\cdot\hat{\mathbf{t}}(\tilde{\mathbf{r}}')|\tilde{\mathbf{r}}-\tilde{\mathbf{r}}'|\,d\tilde l'\,d\tilde l > 0; \tag{24}$$

we have chosen $l_c = \Gamma/2\pi$. Using Eq. (9) and the Binet-Cauchy identity, Eq. (22) becomes

$$\kappa_0^{(3)} = i(\kappa_0^\perp)^2\frac{1}{6\pi}\|\mathbf{P}_M\|^2, \tag{25}$$

where $\mathbf{P}_M$ is the magnetic dipole moment of the mode in the scaled object,

$$\mathbf{P}_M = \frac{1}{2}\int_{\tilde\Omega}\tilde{\mathbf{r}}\times\mathbf{j}_0\,d\tilde V. \tag{26}$$

The radiation quality factor is given by

$$Q = \frac{6\pi}{\kappa_0^\perp\|\mathbf{P}_M\|^2}\frac{1}{x_0^3}, \tag{27}$$

where $x_0 = \omega_0/\omega_c$ and $\omega_0$ is the resonance frequency; it is solution of Eq. (6) and takes into account the radiative shift. These corrections well describe the position of the resonance frequency and the quality factor for $x \lesssim 1$.

The expression of the induced polarization current in the loop with the radiative corrections is obtained by substituting $\kappa_0^\perp$ with $\kappa_0 = \kappa_0^\perp + \kappa_0^{(2)}x^2 + \kappa_0^{(3)}x^3$ into Eq. (20).

### D. Circular loop

To illustrate the use of the formulas derived above, we now consider a circular loop with circular cross section (torus), minor radius $r_w$, and major radius $a$. Hollow nanodiscs have recently been used to tailor the magnetic dipole emission [29]. The circular loop was the platform where dielectric resonances were first proposed [1], and its modes were studied in Refs. [17,30]. A circuit model of the dielectric circular loop has been proposed in Ref. [31], and bulk metamaterials made of rings have also been investigated [32].

For a circular loop,

$$\kappa_0^{\perp} = \frac{2a^2}{r_w^2}\frac{a\mu_0}{L}, \tag{28}$$

where $L$ is the inductance of the loop [20],

$$L = \mu_0\sqrt{a(a-r_w)}\left[\left(\frac{2}{k} - k\right)K(k^2) - \frac{2}{k}E(k^2)\right] + \frac{\mu_0}{4}a, \tag{29}$$

where

$$k = \sqrt{\frac{4a(a-r_w)}{(2a-r_w)^2}}, \tag{30}$$

and $K(\cdot)$ and $E(\cdot)$ are the complete elliptic integrals of the first and second kinds [33]. The term $\mu_0/4a$ in Eq. (29) is the internal inductance of the loop [20]. The expression of the second-order correction follows from Eq. (23):

$$\kappa_0^{(2)} = -\frac{2}{3}\frac{2a^2}{r_w^2}\left(\frac{a\mu_0}{L}\right)^2. \tag{31}$$

Therefore, for a nondispersive material, the expression of the resonance frequency is obtained from Eq. (6):

$$\omega_0 = \frac{c_0}{a}\left[\sqrt{\frac{r_w^2}{2a^2}\left(\frac{L}{a\mu_0}\right)\mathrm{Re}\{\chi\} + \frac{2}{3}\left(\frac{a\mu_0}{L}\right)}\right]^{-1}. \tag{32}$$

The expression of the radiative quality factor is given by

$$Q = \frac{6}{\pi}\left(\frac{L}{a\mu_0}\right)\frac{1}{x_0^3}. \tag{33}$$

We have validated Eqs. (32) and (33) against COMSOL Multiphysics® (wave optics package) considering a high-permittivity loop with $r_w = 0.1a$. Specifically, in Fig. 2, we compare the resonance position obtained by Eq. (32) against the position of the resonance peak of the scattering spectrum computed in COMSOL, when the loop is excited by an electric point dipole, located in the equatorial plane of the loop, at a distance $3a$ from the center, and oriented along the toroidal direction. We find very good agreement for very high permittivities, while the error slightly deteriorates for smaller values of permittivity where the dimension of the object becomes comparable to the resonance wavelength.

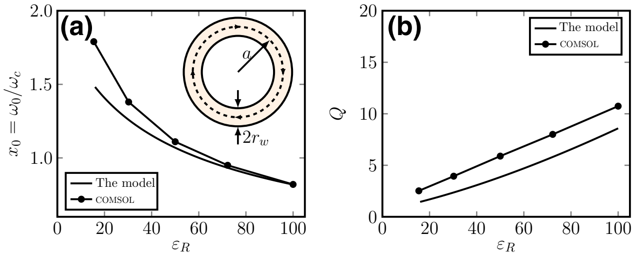

FIG. 2. Comparison between the proposed model and COMSOL. (a) Resonance frequency normalized to $\omega_c = c_0/a$, that is, $x_0 = \omega_0/\omega_c$, and (b) radiative quality factor $Q$ of a high-permittivity circular loop with major radius $a$ and minor radius $r_w = 0.1a$ as a function of the permittivity $\varepsilon_R$.

In Fig. 2(b) we compare the quality factor obtained with Eq. (33) against the inverse of the fractional bandwidth, namely the ratio of the full width at half maximum to the peak frequency, obtained in COMSOL. Good agreement is found.

We observe that the resonant position and the $Q$ factor are slightly underestimated by the model, because, for $x_0 \approx 1$, the radiative effects are significant. Nevertheless, the introduced corrections [first real and imaginary nonvanishing terms in Eq. (5)] quantitatively predict the behavior of the resonance position as $\varepsilon_R$ varies. In addition to the radiative effects, in the thin-wire approximation, we assumed the polarization current to be uniform on the cross section of the wire. In reality, the fundamental magnetoquasistatic mode of this structure is more concentrated near the wire's axis, as shown in Ref. [17].

## IV. TWO INTERACTING HIGH-PERMITTIVITY LOOPS

In this section, we consider a pair of high-permittivity thin-wire loops occupying two disjoint spatial domains $\Omega_1$ and $\Omega_2$ with cross sections $\Sigma_1$ and $\Sigma_2$. The wire axes are represented by the closed curves $\Gamma_1$ and $\Gamma_2$ with tangent unit vectors $\hat{\mathbf{t}}_1$ and $\hat{\mathbf{t}}_2$, respectively. The polarization current density in each loop is uniformly distributed across the wire cross section and directed along its axis; $I_1$ and $I_2$ are respectively the polarization current intensities of the two loops.

### A. Lumped-element model for a loop pair

By following the procedure introduced in Sec. III B, we obtain the following system of equations for the intensities of the induced polarization currents (the lumped-element circuit is shown in Fig. 3):

$$\begin{aligned} i\omega L_1 I_1 + i\omega M I_2 + \frac{1}{i\chi\omega C_1} I_1 &= \mathcal{E}_{\text{ext},1}, \\ i\omega M I_1 + i\omega L_2 I_2 + \frac{1}{i\chi\omega C_2} I_2 &= \mathcal{E}_{\text{ext},2}. \end{aligned} \tag{34}$$

Here

$$C_q = \varepsilon_0 \frac{\Sigma_q}{\Gamma_q}, \qquad q \in 1, 2, \tag{35}$$

$L_1$ and $L_2$ are the self inductances of the loops, and $M$ is the mutual inductance between the two loops,

$$M = \frac{\mu_0}{4\pi} \oint_{\Gamma_1} \oint_{\Gamma_2} \frac{\hat{\mathbf{t}}_1 \cdot \hat{\mathbf{t}}_2}{|\mathbf{r} - \mathbf{r}'|}\, dl_1\, dl_2. \tag{36}$$

The modes of the loop pair are solutions of the generalized eigenvalue problem

$$\underline{\underline{L}}\,\underline{u} = \frac{1}{\kappa^\perp} \frac{1}{\omega_c^2} \underline{\underline{C}}^{-1} \underline{u}, \tag{37}$$

where

$$\underline{\underline{L}} = \begin{pmatrix} L_1 & M \\ M & L_2 \end{pmatrix} \tag{38}$$

and

$$\underline{\underline{C}} = \begin{pmatrix} C_1 & 0 \\ 0 & C_2 \end{pmatrix}. \tag{39}$$

The generalized eigenvalue problem has two eigenvalues, $\kappa_\pm^\perp$, and two current modes, $\underline{u}_\pm$. These modes exhibit equidirected and counterdirected currents, which are called *Helmholtz* and *anti-Helmholtz* modes, respectively. They are orthogonal according to the weighted scalar product $\underline{u}_\pm^\intercal \underline{\underline{C}}^{-1} \underline{u}_\mp = 0$ and are normalized as

$$\varepsilon_0 l_c\, \underline{u}_\pm^\intercal \underline{\underline{C}}^{-1} \underline{u}_\pm = 1. \tag{40}$$

Since the magnetic energy of each current mode is strictly definite positive, the matrix $\underline{\underline{L}}$ is strictly definite positive; thus, $L_1 L_2 > M^2$. The solution of problem (34) in terms of the current modes is

$$\underline{I} = i\varepsilon_0 \omega \chi l_c \sum_{h=\pm} \frac{\underline{u}_h^\intercal \underline{\mathcal{E}}_{\text{ext}}}{1 - x^2 \chi / \kappa_h^\perp} \underline{u}_h, \tag{41}$$

where $\underline{\mathcal{E}}_{\text{ext}} = (\mathcal{E}_{1,\text{ext}}, \mathcal{E}_{2,\text{ext}})^\intercal$ and $\underline{I} = (I_1, I_2)^\intercal$.

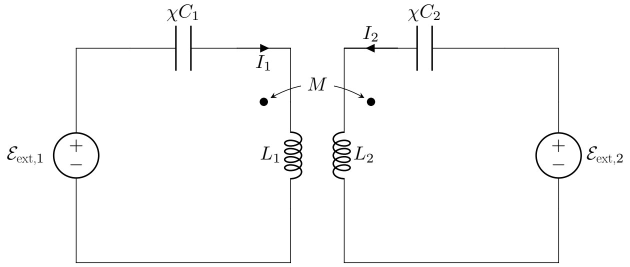

FIG. 3. Lumped-element circuit for two mutually coupled high-permittivity loops.

### B. Radiative corrections

The second-order corrections to $\kappa_\pm^\perp$ are given by

$$\kappa_\pm^{(2)} = \frac{(\kappa_\pm^\perp)^2}{8\pi} \underline{u}_\pm^\intercal \underline{\underline{\Delta}}^{(2)} \underline{u}_\pm, \tag{42}$$

and the first nonvanishing imaginary corrections (of odd order $n_i \geq 3$) are given by

$$\kappa_\pm^{(n_i)} = i(-1)^{(n_i-1)/2} \frac{(\kappa_\pm^\perp)^2}{4\pi n_i!} \underline{u}_\pm^\intercal \underline{\underline{\Delta}}^{(n_i)} \underline{u}_\pm, \tag{43}$$

where the elements of the matrix $\underline{\underline{\Delta}}^{(n)}$ are

$$\left(\underline{\underline{\Delta}}^{(n)}\right)_{pq} = \oint_{\tilde{\Gamma}_p} \oint_{\tilde{\Gamma}_q} \hat{\mathbf{t}}_p(\tilde{\mathbf{r}}) \cdot \hat{\mathbf{t}}_q(\tilde{\mathbf{r}}') |\tilde{\mathbf{r}} - \tilde{\mathbf{r}}'|^{n-1}\, d\tilde{l}'\, d\tilde{l}. \tag{44}$$

For loops with different shapes and/or sizes, the first nonvanishing imaginary corrections for both the modes is 3. If the two loops are equal, the first nonvanishing imaginary corrections for the *anti-Helmholtz* mode is 5.

As for the single loop, these corrections describe the position of the resonance frequency and the quality factor for $x \lesssim 1$. They also take into account the radiative coupling between the two loops.

The expression of the induced polarization currents in the loop pair with the radiative corrections is obtained by substituting $\kappa_\pm^\perp$ with $\kappa_\pm = \kappa_\pm^\perp + \kappa_\pm^{(2)} x^2 + i\kappa_\pm^{(n_i)} x^{n_i}$ into Eq. (41).

### C. Two coaxial circular loops

We now consider two coaxial circular loops with the same permittivity $\varepsilon_R$, circular cross sections, major radii $a$ and $b$, equal minor radius $r_w$, and axial distance $d$, as sketched in Fig. 4(a). The self-inductances $L_1$ and $L_2$ are given by Eq. (29) and the mutual inductance is given by [22,34]

$$M = \mu_0 \sqrt{ab} \left[ \left( \frac{2}{k'} - k' \right) K(k'^2) - \frac{2}{k'} E(k'^2) \right], \tag{45}$$

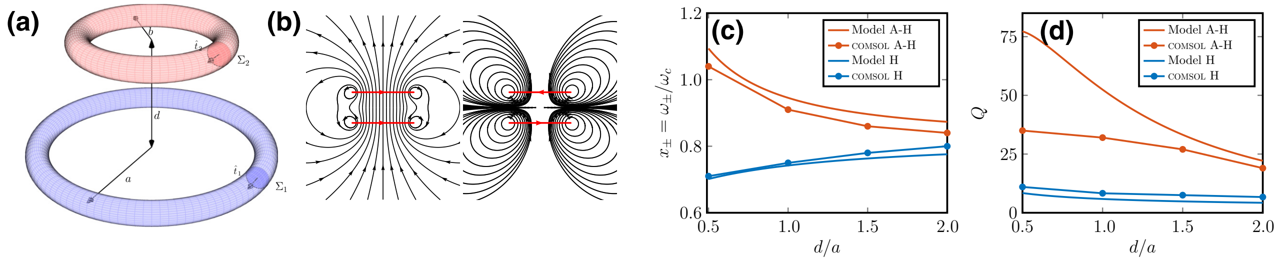

FIG. 4. (a) Two loops with major radii $a$ and $b$, distance $d$, sections $\Sigma_1$ and $\Sigma_2$. (b) Magnetic field lines generated by Helmholtz (H) and anti-Helmholtz (A-H) current modes for $a = b$ and $d = a/2$. (c),(d) Comparison between the results obtained by the proposed model and by COMSOL, assuming that $\varepsilon_R = 100$: resonance frequency (c) normalized to $\omega_c = c_0/a$, $x_\pm = \omega_\pm/\omega_c$ and radiative quality factor (d).

where $K(k)$ and $E(k)$ are the complete elliptic integrals of the first and second kinds, and

$$k' = \sqrt{\frac{4ab}{(a+b)^2 + d^2}}. \tag{46}$$

Figure 4(b) shows the field lines of the magnetic field generated by the Helmholtz $\underline{u}_-$ and anti-Helmholtz $\underline{u}_+$ current modes for $a = b$. Figure 4(c) shows the resonance frequencies of these modes normalized to $\omega_c$, $x_\pm = \omega_\pm/\omega_c$, as a function of the distance between the loops $d$, for $r_w = 0.1a$ and $\varepsilon_R = 100$. The red and blue full lines respectively represent the resonance frequencies of the anti-Helmholtz and Helmholtz current modes. We validate them with the peak position of the scattering response evaluated with COMSOL when the two loops are excited by an electric point dipole (red and blue lines with dots) located in the equatorial plane of the loop of major radius $a$, at a distance $3a$ from its center, oriented along its toroidal direction. The agreement is good, even though the anti-Helmholtz mode experiences a larger error because $x_+ \approx 1$. Figure 4(d) compares the quality factor (7) against the inverse of the fractional bandwidth obtained in COMSOL as a function of the loop distance. We find good agreement for the Helmholtz mode. For the anti-Helmholtz mode, the overall magnetic dipole moment is vanishing, and thus $\kappa_h^{(3)} = 0$, and the quadrupole contribution ($n_i = 5$) has to be considered. For values $d/a > 1.5$, we find quantitative agreement. Nevertheless, as the distance $d$ between the two loops decreases, the error increases. This is because Eq. (45) does not take into account the finite size of the wires, and becomes inaccurate for small values of $d/a$, when the two loops exhibit a strong near-field interaction. The quality factor of the anti-Helmholtz mode is more sensitive to the approximations we made because, according to Eq. (7), it depends on the fifth power of the normalized resonance frequency $x_+$, whereas for the Helmholtz mode, it depends on the third power of $x_-$. The resonance frequency is more robust because the quasistatic approximation alone is able to estimate its order of magnitude, and the correction only enters with the second power of the size parameter $x_\pm$.

## V. HIGH-PERMITTIVITY DIELECTRIC NETWORK

In this section, we generalize the concepts introduced so far by considering an arbitrary interconnection of high-permittivity thin wires, e.g., Fig. 5. The lumped-element model we propose allows us to study the main properties of the electromagnetic scattering from such structures: in particular, the induced polarization currents expressed in terms of the magnetoquasistatic current modes, their resonance frequencies, their radiative frequency shifts, and their radiative quality factors.

In the magnetoquasistatic limit the normal component of the polarization current density vanishes at the object's surface; hence, there is not *leakage* of the polarization current density. Therefore, at each node of the network the sum of the polarization current intensity is conserved, analogous to Kirchhoff's law for electric currents [35]. Under the considered hypotheses, wires extending out of a loop or connecting two disjoint loops only weakly influence

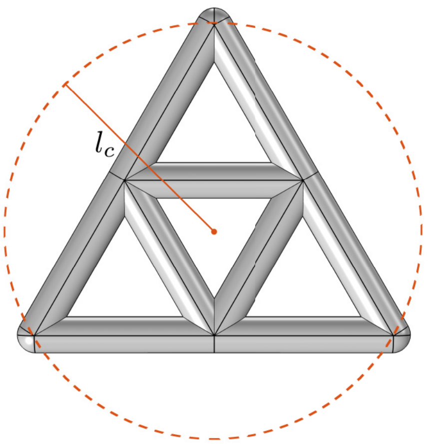

FIG. 5. Top view of an exemplification of a dielectric network.

the scattering from high-permittivity dielectric networks. Thus, if present, they can be pruned before applying the loop analysis of the following sections.

### A. Network digraph

As for electric circuits [35], it is convenient to associate with the dielectric network a digraph $\mathcal{G}$, i.e., an oriented graph, with $n$ nodes and $b$ branches. We denote with $e_h$ the $h$th branch of the digraph, $\hat{\mathbf{t}}_h$ its tangent unit vector, and $I_h$ the intensity of the branch polarization current. The digraph associated with the network of Fig. 5 is shown in the top layer of Fig. 6. For simplicity, we restrict our analysis to connected graphs. If the graph is not connected, one may simply combine the following approach with that carried out in the previous section.

A loop $\mathcal{L}_i$ of $\mathcal{G}$ is a connected subgraph where exactly two branches are incident in each node. A tree $\mathcal{T}$ of a connected digraph $\mathcal{G}$ is a connected subgraph that contains all the nodes of $\mathcal{G}$, but no loop. For any given digraph $\mathcal{G}$, many possible choices of trees are possible. Given a connected digraph and a chosen tree, the branches of $\mathcal{G}$ are partitioned into two disjoint sets: those belonging to $\mathcal{T}$, called *twigs*, and those that do not belong to $\mathcal{T}$, called *links*. The *fundamental theorem of graphs* [35] states that, given a connected graph with $n$ nodes and $b$ branches and a tree $\mathcal{T}$, there are $n-1$ twigs and $\ell = b-(n-1)$ links. Every link (e.g., the $p$th link) together with a proper choice of twigs constitutes a unique loop, called the fundamental loop associated with the link. For instance, considering the graph shown in the top layer of Fig. 6 we can associate to every link of the particular tree $\mathcal{T}$ highlighted in red the four fundamental loops $\mathcal{L}_1, \ldots, \mathcal{L}_4$, shown in the layers below. Their orientation is defined by the direction of the corresponding link.

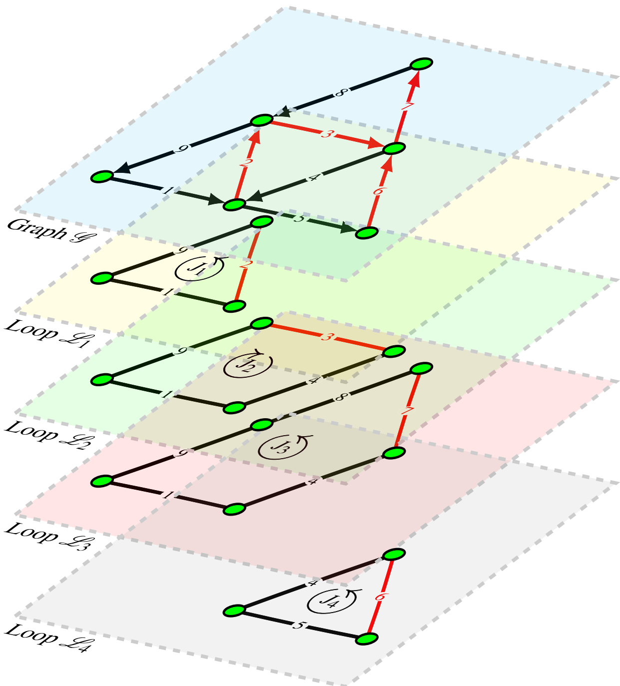

FIG. 6. Top layer: graph $\mathcal{G}$ associated with the dielectric network shown in Fig. 5; the chosen tree $\mathcal{T}$ is highlighted black and the corresponding links are highlighted red. Layers below: fundamental loops $\mathcal{L}_1$–$\mathcal{L}_4$ associated with the four different links. Their orientation is defined by the direction of the corresponding link.

A set of fundamental loops is identified through the $\ell \times b$ fundamental loop matrix $\underline{\underline{B}}$ associated with the corresponding tree. The $jk$ occurrence is defined as follows: $b_{jk} = 1$ if branch $k$ is in loop $j$ and their reference directions are the same; $b_{jk} = -1$ if branch $k$ is in loop $j$ and their reference directions are opposite; $b_{jk} = 0$ if branch $k$ is not in loop $j$.

### B. General lumped-element model

We now use the *loop analysis* to formulate the electromagnetic scattering problem from the dielectric network: the $b$ polarization current intensities of the network are expressed in terms of the $\ell$ fundamental loop currents. This choice guarantees that the polarization currents satisfy Kirchhoff's law at any node of the digraph.

Let be $\underline{I}$ the (column) vector representing the polarization current intensities of the branches of the circuit $\{I_1, I_2, \ldots, I_b\}$, and let $\underline{J}$ be the column vector representing the current intensities of the links associated with the tree $\mathcal{T}$ of the circuit, $\{J_1, J_2, \ldots, J_\ell\}$. The conservation of the sum of the polarization currents at the nodes of the circuit implies that [35]

$$\underline{I} = \underline{\underline{B}}^{\intercal}\underline{J}. \tag{47}$$

Let $\underline{\mathcal{E}}$ be the column vector representing the set of induced loop voltages $\{\mathcal{E}_1, \mathcal{E}_2, \ldots, \mathcal{E}_\ell\}$, and let $\underline{\mathcal{E}}_{\text{ext}}$ be the column vector representing the set of loop external voltages $\{\mathcal{E}_{\text{ext},1}, \mathcal{E}_{\text{ext},2}, \ldots, \mathcal{E}_{\text{ext},\ell}\}$. The constitutive relations of the dielectric thin wires gives [by performing the line integral of Eq. (12) along each fundamental loop]

$$\frac{1}{\chi}\underline{\underline{B}}(i\omega\underline{\underline{C}})^{-1}\underline{I} = \underline{\mathcal{E}} + \underline{\mathcal{E}}_{\text{ext}}, \tag{48}$$

where $\underline{\underline{C}}$ is the diagonal matrix whose elements are $C_h = (\varepsilon_0 \Sigma_h)/\Gamma_h$ with $h = 1, 2, \ldots, b$, $\Sigma_h$ is the cross section of the $h$th wire (edge), and $\Gamma_h$ is the length. On the other hand, the Faraday law gives

$$\underline{\mathcal{E}} = -i\omega\underline{\underline{L}}\,\underline{J}, \tag{49}$$

where $\underline{\underline{L}}$ is the $\ell \times \ell$ inductance matrix of the set of fundamental loops. By combining Eqs. (47)–(49) we obtain the system of equations governing the set of link currents associated with the tree $\mathcal{T}$,

$$i\omega\underline{\underline{L}}\,\underline{J} + \frac{1}{i\omega\chi}\underline{\underline{B}}\,\underline{\underline{C}}^{-1}\underline{\underline{B}}^{\intercal}\underline{J} = \underline{\mathcal{E}}_{\text{ext}}. \tag{50}$$

The current modes $\{\underline{u}_h\}$ of the network and the corresponding eigenvalues $\{\kappa_h^{\perp}\}$ are solutions of the generalized eigenvalue problem

$$\underline{\underline{L}}\,\underline{u} = \frac{1}{\kappa^{\perp}}\frac{1}{\omega_c^2}\underline{\underline{B}}\,\underline{\underline{C}}^{-1}\underline{\underline{B}}^{\intercal}\,\underline{u}. \tag{51}$$

The number of magnetoquasistatic current modes and of resonances of a high-permittivity dielectric network is equal to the number of links $\ell$ of the digraph $\mathcal{G}$ of the network. The matrices $\underline{\underline{L}}$ and $\underline{\underline{B}}\,\underline{\underline{C}}^{-1}\underline{\underline{B}}^{\intercal}$ are symmetric and definite positive. As a consequence, the eigenvalues $\{\kappa_h^{\perp}\}$ are real and positive, and the current modes satisfy a weighted orthogonality,

$$\varepsilon_0 l_c \underline{u}_h^{\intercal}(\underline{\underline{B}}\,\underline{\underline{C}}^{-1}\underline{\underline{B}}^{\intercal})\underline{u}_k = \delta_{hk}. \tag{52}$$

The solution of Eq. (50) is

$$\underline{J} = i\varepsilon_0\omega\chi l_c\sum_{h=1}^{\ell}\frac{\underline{u}_h^{\intercal}\underline{\mathcal{E}}_{\text{ext}}}{1-x^2\chi/\kappa_h^{\perp}}\underline{u}_h. \tag{53}$$

### C. Partial inductances

The direct calculation of self- and mutual inductances of fundamental loops may not be the most efficient method to assemble the matrix $\underline{\underline{L}}$, since different loops may share several branches, resulting in redundant and hence inefficient computations. It is instead convenient, as for electric circuits [20,22], to preliminary assemble the partial loop inductances matrix $\underline{\underline{L}}^{\text{P}}$. Its $ij$ occurrence is the partial inductance $L_{ij}^{\text{P}}$ between the branches $e_i$ and $e_j$. It is defined as the ratio between the magnetic flux produced by the current density flowing in the branch $e_j$, through the surface between the branch $e_i$ and infinity, and the current of the branch $e_j$, namely,

$$L_{ij}^{\text{P}} = \frac{1}{I_j}\int_{e_i}\mathbf{A}_j\cdot\hat{\mathbf{t}}_i\,d\tilde{l}. \tag{54}$$

There are $b(b+1)/2$ independent partial inductances $L_{ij}^{\text{P}}$, because $L_{ij}^{\text{P}} = L_{ji}^{\text{P}}$ by reciprocity. The loop inductance matrix $\underline{\underline{L}}$ is given by

$$\underline{\underline{L}} = \underline{\underline{B}}\,\underline{\underline{L}}^{\text{P}}\,\underline{\underline{B}}^{\intercal}. \tag{55}$$

If the circuit is composed of an arbitrary interconnection of *straight* wires laying on the same plane then we need formulas for calculating (i) self-partial inductance of a straight wire (Appendix A 1); (ii) the mutual-partial inductance between wires at an angle to each other (Appendix A 3) that includes as a limit case the mutual-partial inductance between parallel wires (Appendix A 2), and the mutual-partial inductance of wires meeting in a point (given by Campbell [36]). If the circuit is not planar then the mutual-partial inductance between skewed and displaced wires first derived by Martens and Campbell [20,22,36,37] is also needed.

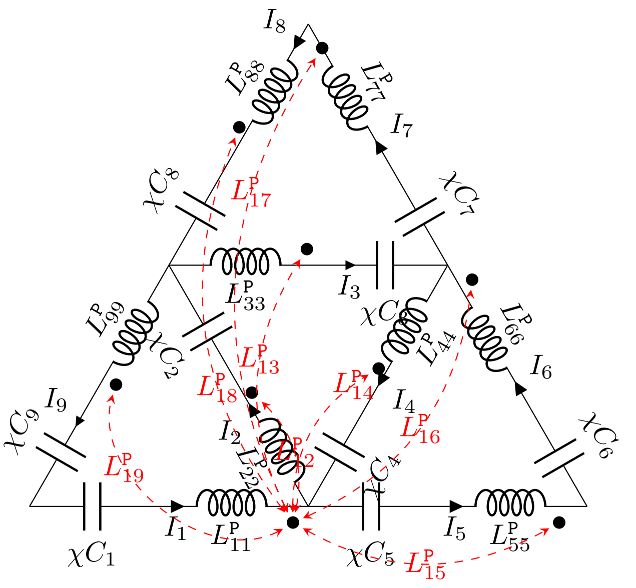

FIG. 7. Lumped-element circuit for the dielectric network in Fig. 5. The self-partial inductances $L_{qq}^{\text{P}}$ of each branch of the digraph are shown. The mutual-partial inductances between the first branch and any other branch are shown in red. The dotted convention commonly employed in magnetically coupled circuits is used in this case.

In Fig. 7 we show the lumped circuit for the dielectric network shown in Fig. 5, where we illustrate the self-partial inductances $L_{qq}^{\text{P}}$, and, for sake of clarity, only the mutual-partial inductance $L_{1q}^{\text{P}}$.

### D. Radiative corrections

The expression of the second-order (real) radiative correction for the $h$th mode is

$$\kappa_h^{(2)} = \frac{(\kappa_h^{\perp})^2}{8\pi}\underline{u}_h^{\intercal}\underline{\underline{B}}\,\underline{\underline{\Delta}}^{(2)}\,\underline{\underline{B}}^{\intercal}\underline{u}_h, \tag{56}$$

and the expression of the lowest order $n_i$ imaginary correction (which is an odd number $n_i \geq 3$) is

$$\kappa_h^{(n_i)} = i(-1)^{(n_i-1)/2}\frac{(\kappa_h^{\perp})^2}{4\pi n_i!}\underline{u}_h^{\intercal}\,\underline{\underline{B}}\,\underline{\underline{\Delta}}^{(n_i)}\,\underline{\underline{B}}^{\intercal}\underline{u}_h, \tag{57}$$

where the elements of the matrix $\underline{\underline{\Delta}}^{(n)}$ are

$$\left(\underline{\underline{\Delta}}^{(n)}\right)_{ij} = \oint_{\tilde{e}_i} \hat{\mathbf{t}}_i(\tilde{\mathbf{r}}) \cdot \oint_{\tilde{e}_j} \hat{\mathbf{t}}_j(\tilde{\mathbf{r}}')|\tilde{\mathbf{r}} - \tilde{\mathbf{r}}'|^{n-1}\, d\tilde{l}'\, d\tilde{l}. \qquad (58)$$

Also, in this case, these corrections describe the position of the resonance frequency and the quality factor for $x \lesssim 1$. They take into account the radiative coupling among the network's loops.

The expression of the induced polarization currents in the links of the dielectric network taking into account the radiative corrections is obtained by substituting $\kappa_h^{\perp}$ with $\kappa_h = \kappa_h^{\perp} + \kappa_h^{(2)}x^2 + i\kappa_h^{(n_i)}x^{n_i}$ for $h = 1, \ldots, \ell$ into Eq. (53).

### E. Sierpinski triangle

Let us analyze the dielectric network shown in Fig. 5, composed of $b = 9$ high-permittivity thin wires of equal length $l_w$, with circular cross section of radius $r_w = 0.1 l_w$. The wires are interconnected according to a Sierpinski triangle [38]. The minimum circle circumscribing the network is chosen as the characteristic length $l_c$.

The graph of this network is shown in the top layer of Fig. 6, where the twigs and links, associated with a chosen tree, are highlighted in red and black, respectively. The fundamental loops associated with each *link* are shown in the layers below. The lumped-element circuit is shown in Fig. 7. The 45 independent partial inductances are evaluated first, then the 10 independent elements of the $4 \times 4$ symmetric inductance matrix $\underline{\underline{L}}$ are computed. In this simple case, the calculation of the eigenvalues $\kappa_h^{(2)}$ can be carried out with pen and paper, returning the four values listed in Table I. The four current modes are shown in Fig. 8 (the second and the third modes are degenerate). These modes correspond to the magnetoquasistatic current density modes reported in Fig. 8. Then, the matrices $\underline{\underline{\Delta}}^{(2)}$ and $\underline{\underline{\Delta}}^{(n_i)}$ are assembled, where $n_i = 3$ for the first and fourth modes, and $n_i = 5$ for the second and third modes. The radiation corrections $\kappa_h^{(2)}$ and $\kappa_h^{(n_i)}$ are given in Table I.

Table II gives the normalized resonance frequencies and the quality factors of the four current modes of the Sierpinski network for two different values of the permittivity, $\varepsilon_R = 100$ and $\varepsilon_R = 15.45$. For $\varepsilon_R = 100$, the first (fundamental) resonance is located at $x_1 = 1.08$: for $l_c = 10$ cm, it is $\omega_1 = 3.25$ GHz. The scattering peak positions and the quality factors of the four current modes have also been estimated using COMSOL Multiphysics. The dielectric network shown in Fig. 5 has been excited by an electric dipole, laying on its equatorial plane, located at $3l_w$ on the left of its center, and oriented along the vertical in-plane direction. The quality factor is estimated as the inverse of the fractional bandwidth. The lumped circuit model exhibits good accuracy in locating the resonances, while returning the order of magnitude of the quality factors. The comparison is repeated for $\varepsilon_R = 15.45$. The first (fundamental) resonance is located at $x_1 = 2.12$; thus, for $l_c = 250$ nm, the resonance wavelength is located within the near-infrared spectral range, $\lambda_1 = 740$ nm. The relative

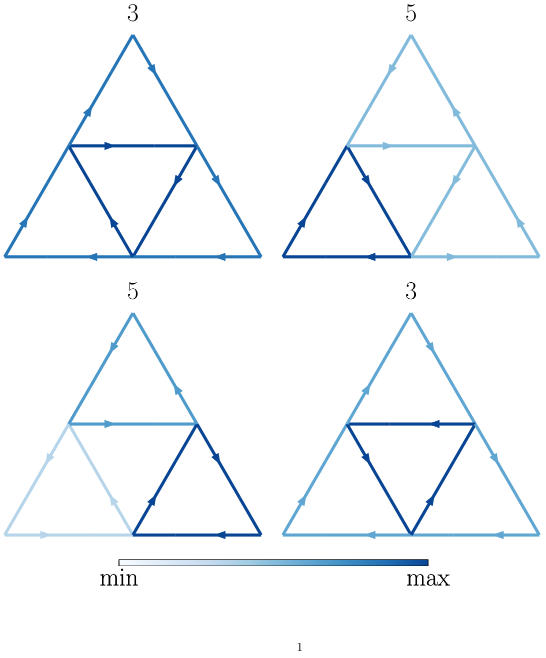

FIG. 8. Current modes of the dielectric network arranged according to a Sierpinski triangle with generation number 1. Each wire has length $l_w$ and radius $r_w = 0.1 l_w$. The modes are arranged in a lexicographic order that follows the corresponding eigenvalue. Above each mode is the order $n_i$ of the first nonvanishing imaginary correction of its magnetoquasistatic eigenvalue.

TABLE I. Eigenvalues $\kappa_h^{\perp}$, second-order (real) radiative correction $\kappa_h^{(2)}$, imaginary correction $\kappa_h^{(n_i)}$ of the lowest order $n_i$ of the dielectric network of Fig. 5.

| | | | | |
|---|---|---|---|---|
| $\kappa_h^{\perp}$ | 134 | 181 | 181 | 379 |
| $\kappa_h^{(2)}$ | −15 | −5.0 | −5.0 | −19.0 |
| $n_i$ | 3 | 5 | 5 | 3 |
| $\kappa_h^{(n_i)}$ | 7.2 | 0.24 | 0.24 | 8.3 |

TABLE II. Normalized resonance frequencies $x_h = \omega_h/\omega_c$ and quality factors of the four modes of the dielectric network of Fig. 5 for $\varepsilon_R = 100$ and $\varepsilon_R = 15.45$.

| | $x_1$ | $x_2 = x_3$ | $x_4$ | $Q_1$ | $Q_2 = Q_3$ | $Q_4$ |
|---|---|---|---|---|---|---|
| | | | $\varepsilon_R = 100$ | | | |
| The model | 1.08 | 1.31 | 1.78 | 15 | 182 | 8.0 |
| COMSOL | 1.04 | 1.26 | ⋯ | 31 | 280 | ⋯ |
| | | | $\varepsilon_R = 15.45$ | | | |
| The model | 2.12 | 3.04 | 3.34 | 1.9 | 2.7 | 1.2 |
| COMSOL | 2.29 | 2.89 | ⋯ | 3.9 | 8.3 | ⋯ |

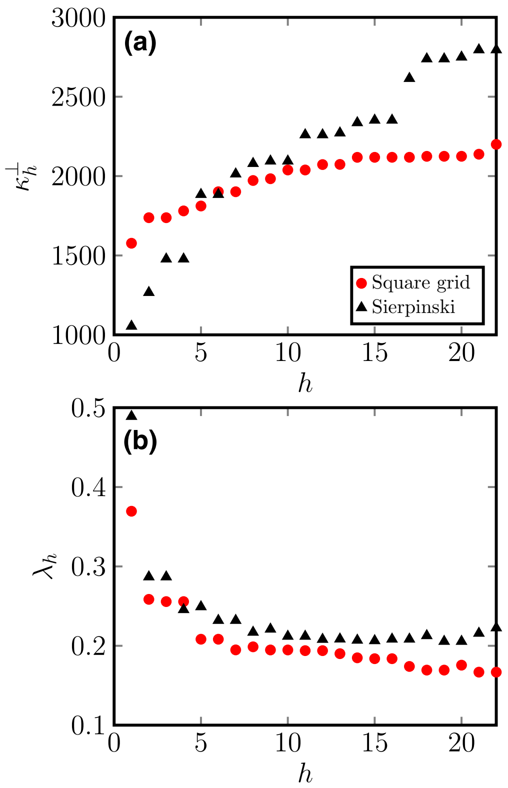

FIG. 9. (a) The first 21 eigenvalues $\kappa_h^{\perp}$ of a Sierpinski triangle (generation number 3) with $b = 81$, $n = 42$, and $\ell = 40$, and the first 21 eigenvalues $\kappa_h^{\perp}$ of a $7 \times 7$ square grid with $b = 112$, $n = 64$, and $\ell = 49$. (b) Corresponding resonance wavelengths (in meters), assuming that $\varepsilon_R = 100$ and $a = 3$ cm.

error in the predicted resonance position (compared to its COMSOL counterpart) worsens on average with respect to the previous scenario, but it remains below the 15%. For both the investigated permittivities, in the COMSOL simulation, the scattering peak associated with the fourth mode is not clearly identifiable, due to its low quality factor. For this reason, the position of its resonance peak and its $Q$ factor estimate are omitted in Table II.

We now illustrate how the analysis of complex dielectric networks may benefit from the use of a lumped-element approach. We investigate two networks: the first is composed of $b = 81$ thin wires interconnected according to a Sierpinski triangle with generation number 3, and the second is instead composed of $b = 112$ thin wires interconnected according to a square grid. The first (smallest) 21 eigenvalues of both the networks are compared in Fig. 9. The corresponding current modes are shown in Figs. 10 and 11. The number reported above each mode is the order $n_i$ of the first nonvanishing imaginary radiative correction. This number returns the power dependence of the quality factor on the size parameter, according to Eq. (7), and it is related to the multipolar components of the mode.

These two networks may be implemented at radio frequencies: assuming that the permittivity $\varepsilon_R = 100$, the smallest edge of both networks is $a = 3$ cm, and that the wire radius $r_w = 3$ mm, we obtain networks of characteristic dimensions $l_c = 13$ cm for a Sierpinski triangle and $l_c = 10.5$ cm for a square grid. The 21 largest resonance wavelengths are shown in Fig. 9(b). The resonance wavelengths of the Sierpinski triangle fall in the range 12–37 cm, which belongs to the ultrahigh frequency band; they are always larger than or at most roughly equal to the characteristic dimension of the structure $l_c = 13$ cm. Similarly, the resonance frequencies of a square grid fall in the range 14–48 cm. Also, in this case they are greater than the dimension of the structure $l_c = 10.5$ cm, thus falling within the domain of validity of this approximation.

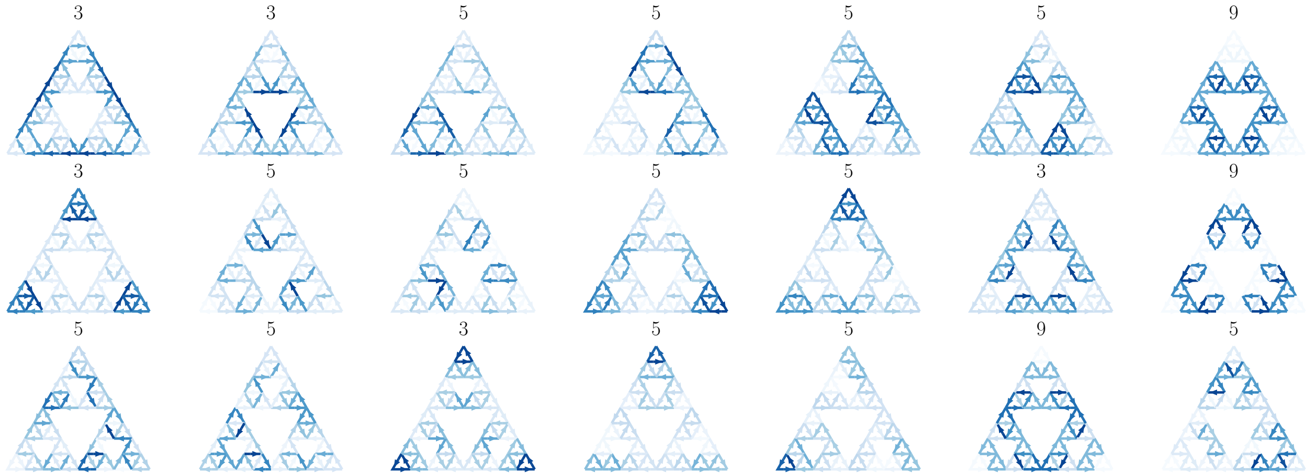

FIG. 10. The first 21 magnetoquasistatic modes of a dielectric network comprising $b = 81$ thin wires interconnected according to a Sierpinski triangle. Each wire has length $a$ and radius $r_w = 0.1a$. The modes are lexicographically ordered in terms of increasing magnetoquasistatic eigenvalues. Above each mode is the order $n_i$ of the first nonvanishing imaginary correction of its magnetoquasistatic eigenvalue.

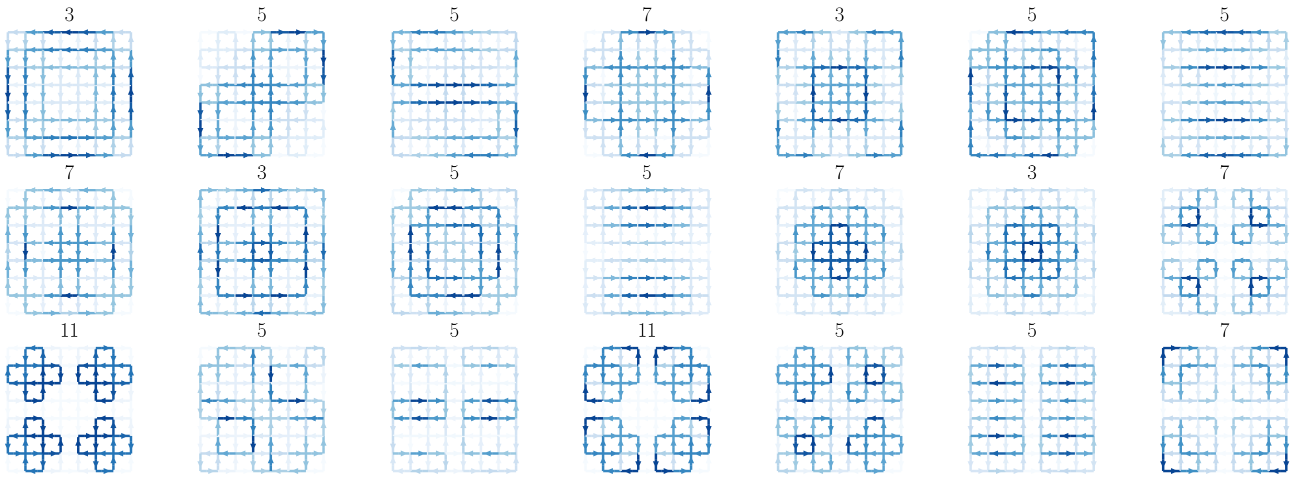

FIG. 11. The first 21 magnetoquasistatic modes of a dielectric network comprising $b = 112$ thin wires arranged according to a square grid. Each wire has length $a$ and radius $r_w = 0.1a$. The modes are arranged in a lexicographic order that follows the increasing magnetoquasistatic eigenvalues. Above each mode is the order $n_i$ of the first nonvanishing imaginary correction of its magnetoquasistatic eigenvalue.

## VI. CONCLUSIONS

We investigate the electromagnetic scattering from *high-permittivity dielectric networks*. They are interconnections of high-permittivity dielectric thin wires. If the overall size of the network is smaller than or at most equal to the operating wavelength, the dielectric network can be modeled as a lumped circuit constituted by capacitances, and self- and mutual-loop inductances. The resonances and resonance modes are related to the spectrum of the loop-inductance matrix and are equal in number to the links of the network's digraph. Closed-form expressions are given for the frequency shifts and quality factors due to the coupling with the radiation. The inductance matrix can be assembled from the *partial* self- and mutual inductances of the constituent wires, transplanting to the electromagnetic scattering theory formulas introduced a century ago for inductive networks. For networks with sizes smaller than or almost equal to the incident wavelength, the error in locating the resonance is acceptable, below 16% in the investigated numerical experiments. The quality factor may be affected by a larger error, especially when it is very high, and thus very sensitive to the polarization current distribution. The error originates mainly from (i) an inadequate treatment of radiation effects when the structure is comparable in size to the incident wavelength, and (ii) the limits of the thin-wire approximation, which manifest either when the cross-sectional radius of the wire is comparable to its length, or when two wires interact in their immediate proximity.

In conclusion, the proposed model is a fast computational tool for preliminary analysis that could be later refined by more accurate tools that are usually associated with a higher computational burden. It may also help the comprehension of lasing in complex photonic graphs and networks [39–42]. This manuscript may also stimulate the grafting of several other ideas and methods from electric and electronic circuits onto the design of high-index resonators in both the microwave and visible spectral ranges. This approach together with that proposed in Ref. [43] represents the first steps toward the derivation of a full-wave treatment of complex networks of wires.

## APPENDIX A: PARTIAL INDUCTANCES CALCULATION

### 1. Self-partial inductance of a straight wire

The self-partial inductance $L^{\mathrm{P}}$ of the wire of Fig. 12 with radius $r_w$ and length $a$ is

$$L^{\mathrm{P}} = \frac{a\mu_0}{2\pi}\left\{\ln\left[\frac{a}{r_w} + \sqrt{\left(\frac{a}{r_w}\right)^2 + 1}\right] - \sqrt{1 + \left(\frac{r_w}{a}\right)^2} + \frac{r_w}{a}\right\} + \frac{\mu_0}{8\pi}a. \tag{A1}$$

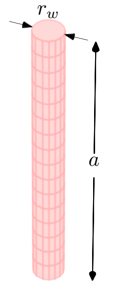

FIG. 12. Self-partial inductance of a wire of length $a$ and circular cross section of radius $r_w$.

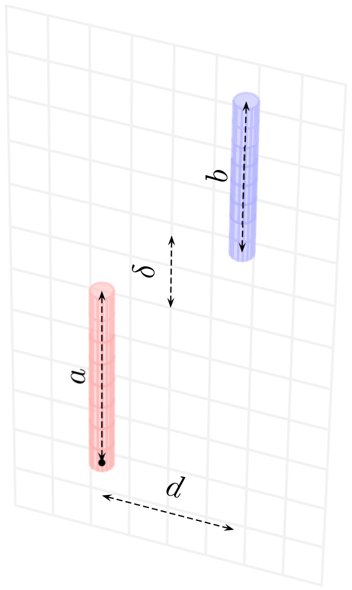

FIG. 13. Mutual-partial inductance of two wires of lengths $a$ and $b$, equal circular cross sections of radius $r_w$, at distance $d$ and offset $z$.

### 2. Mutual-partial inductance between two unequal parallel wires that are offset

The mutual-partial inductance $M^{\mathrm{P}}$ between the two wires shown in Fig. 13 of negligible cross sections, lengths $a$ and $b$, at a distance $d$, and with an offset $\delta$ is given by [22,44]

$$\begin{aligned} M^{\mathrm{P}} = \frac{\mu_0}{4\pi}\bigg( & z_2 \sinh^{-1}\frac{z_2}{d} - z_1 \sinh^{-1}\frac{z_1}{d} - (z_2 - a) \\ & \times \sinh^{-1}\frac{z_2 - a}{d} + (z_1 - a)\sinh^{-1}\frac{z_1 - a}{d} \\ & - \sqrt{z_2^2 + d^2} + \sqrt{z_1^2 + d^2} + \sqrt{(z_2 - a)^2 + d^2} \\ & - \sqrt{(z_1 - a)^2 + d^2}\bigg), \end{aligned} \tag{A2}$$

where $z_2 = a + b + \delta$ and $z_1 = a + \delta$.

### 3. Mutual-partial inductance between wires at an angle to each other

Let us consider the two wires of Fig. 14, of lengths $a$ and $b$, and of negligible cross sections (filaments). The wires are coplanar, forming an angle $\theta$ to each other [20,22,36]. Their mutual inductance is given by

$$\begin{aligned} M^{\mathrm{P}} = \frac{\mu_0}{4\pi}\bigg( & (\beta + b)\ln\frac{r_{24} + r_{14} + a}{r_{24} + r_{14} - a} - \beta\ln\frac{r_{23} + r_{13} + a}{r_{23} + r_{13} - a} \\ & + (a + \alpha)\ln\frac{r_{24} + r_{23} + b}{r_{24} + r_{23} - b} - \alpha\ln\frac{r_{14} + r_{13} + b}{r_{14} + r_{13} - b}\bigg). \end{aligned} \tag{A3}$$

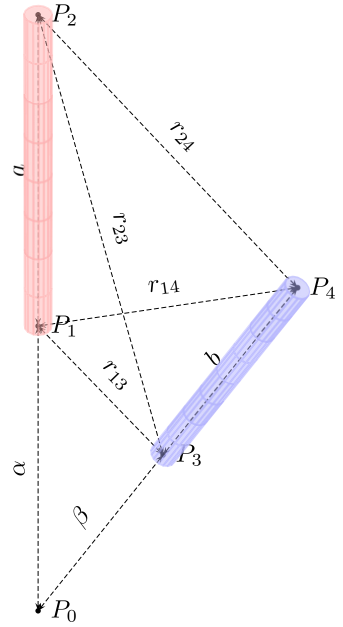

FIG. 14. Mutual-partial inductance of two wires of lengths $a$ and $b$, at an angle to each other.

If the two wires are touching in $P_0$ then the above equation reduces to [36]

$$M^{\mathrm{P}} = \frac{\mu_0}{4\pi}\cos\theta\left(a\ln\frac{r_{24} + a + b}{r_{24} + a - b} + b\ln\frac{r_{24} + a + b}{r_{24} + b - a}\right). \tag{A4}$$

---

[1] R. Richtmyer, Dielectric resonators, J. Appl. Phys. **10**, 391 (1939).

[2] S. Long, M. McAllister, and Liang Shen, The resonant cylindrical dielectric cavity antenna, IEEE Trans. Antennas Propag. **31**, 406 (1983).

[3] O. Yavas, M. Svedendahl, P. Dobosz, V. Sanz, and R. Quidant, On-a-chip biosensing based on all-dielectric nanoresonators, Nano Lett. **17**, 4421 (2017).

[4] A. Karalis, J. D. Joannopoulos, and M. Soljačić, Efficient wireless non-radiative mid-range energy transfer, Ann. Phys. **323**, 34 (2008).

[5] K. Koshelev, S. Kruk, E. Melik-Gaykazyan, J.-H. Choi, A. Bogdanov, H.-G. Park, and Y. Kivshar, Subwavelength dielectric resonators for nonlinear nanophotonics, Science **367**, 288 (2020).

[6] C. L. Holloway, E. F. Kuester, J. Baker-Jarvis, and P. Kabos, A double negative (DNG) composite medium composed of magnetodielectric spherical particles embedded in a matrix, IEEE Trans. Antennas Propag. **51**, 2596 (2003).

[7] R. J. Cava, Dielectric materials for applications in microwave communications basis of a presentation given at materials discussion no. 3, 26–29 September, 2000, University of Cambridge, UK., J. Mater. Chem. **11**, 54 (2001).

[8] I. M. Reaney and D. Iddles, Microwave dielectric ceramics for resonators and filters in mobile phone networks, J. Am. Ceram. Soc. **89**, 2063 (2006).

[9] D. Helena, A. Ramos, T. Varum, and J. N. Matos, Antenna design using modern additive manufacturing technology: A review, IEEE Access **8**, 177064 (2020).

[10] D. G. Baranov, D. A. Zuev, S. I. Lepeshov, O. V. Kotov, A. E. Krasnok, A. B. Evlyukhin, and B. N. Chichkov, All-dielectric nanophotonics: The quest for better materials and fabrication techniques, Optica **4**, 814 (2017).

[11] J. B. Pendry, A. J. Holden, D. J. Robbins, and W. J. Stewart, Low frequency plasmons in thin-wire structures, J. Phys.: Condens. Matter **10**, 4785 (1998).

[12] C. R. Simovski, P. A. Belov, A. V. Atrashchenko, and Y. S. Kivshar, Wire metamaterials: Physics and applications, Adv. Mater. **24**, 4229 (2012).

[13] M. S. Mirmoosa, S. Y. Kosulnikov, and C. R. Simovski, Magnetic hyperbolic metamaterial of high-index nanowires, Phys. Rev. B **94**, 075138 (2016).

[14] G. T. Papadakis, D. Fleischman, A. Davoyan, P. Yeh, and H. A. Atwater, Optical magnetism in planar metamaterial heterostructures, Nat. Commun. **9**, 296 (2018).

[15] G. Mazingue, B. Byrne, M. Romier, and N. Capet, in *2020 14th European Conference on Antennas and Propagation (EuCAP)* (IEEE Institute of Electrical and Electronics Engineers, Copenhagen, Denmark, 2020), p. 1.

[16] C. Forestiere, G. Gravina, G. Miano, M. Pascale, and R. Tricarico, Electromagnetic modes and resonances of two-dimensional bodies, Phys. Rev. B **99**, 155423 (2019).

[17] C. Forestiere, G. Miano, G. Rubinacci, M. Pascale, A. Tamburrino, R. Tricarico, and S. Ventre, Magnetoquasistatic resonances of small dielectric objects, Phys. Rev. Res. **2**, 013158 (2020).

[18] C. Forestiere, G. Miano, and G. Rubinacci, Resonance frequency and radiative Q-factor of plasmonic and dieletric modes of small objects, Phys. Rev. Res. **2**, 043176 (2020).

[19] J. V. Bladel, On the resonances of a dielectric resonator of very high permittivity, IEEE Trans. Microw. Theory Tech. **23**, 199 (1975).

[20] C. R. Paul, *Inductance: Loop and Partial* (John Wiley & Sons, Hoboken, New Jersey (USA), 2011).

[21] E. B. Rosa, *The Self and Mutual Inductances of Linear Conductors* (US Department of Commerce and Labor, Bureau of Standards, Washington, 1908), Vol. 18.

[22] F. W. Grover, *Inductance Calculations: Working Formulas and Tables* (Courier Corporation, New York, 2004).

[23] E. Weber, *Electromagnetic Fields: Theory and Applications* (Wiley, New York, 1950).

[24] N. Engheta, A. Salandrino, and A. Alu, Circuit Elements at Optical Frequencies: Nanoinductors, Nanocapacitors, and Nanoresistors, Phys. Rev. Lett. **95**, 095504 (2005).

[25] A. Alù and N. Engheta, Optical 'shorting wires', Opt. Express **15**, 13773 (2007).

[26] A. Alù, A. Salandrino, and N. Engheta, Parallel, series, and intermediate interconnections of optical nanocircuit elements. 2. Nanocircuit and physical interpretation, J. Opt. Soc. Am. B **24**, 3014 (2007).

[27] A. Salandrino, A. Alù, and N. Engheta, Parallel, series, and intermediate interconnections of optical nanocircuit elements. 1. Analytical solution, J. Opt. Soc. Am. B **24**, 3007 (2007).

[28] J. V. Bladel, Hierarchy of terms in a multipole expansion, Electron. Lett. **24**, 492 (1988).

[29] T. Feng, Y. Xu, Z. Liang, and W. Zhang, All-dielectric hollow nanodisk for tailoring magnetic dipole emission, Opt. Lett. **41**, 5011 (2016).

[30] M. Verplanken and J. V. Bladel, The magnetic-dipole resonances of ring resonators of very high permittivity, IEEE Trans. Microw. Theory Tech. **27**, 328 (1979).

[31] L. Jelinek and R. Marqués, Artificial magnetism and left-handed media from dielectric rings and rods, J. Phys.: Condens. Matter **22**, 025902 (2009).

[32] R. Marques, L. Jelinek, M. J. Freire, J. D. Baena, and M. Lapine, Bulk metamaterials made of resonant rings, Proc. IEEE **99**, 1660 (2011).

[33] M. Abramowitz and I. A. Stegun, *Handbook of Mathematical Functions with Formulas, Graphs, and Mathematical Tables* (Dover, New York, 1964), 9th dover printing ed.

[34] J. C. Maxwell, *A Treatise on Electricity and Magnetism* (Clarendon Press, Oxford, 1873), Vol. II.

[35] L. O. Chua, C. A. Desoer, and E. S. Kuh, *Linear and Nonlinear Circuits* (McGraw-Hill, New York, 1987).

[36] G. A. Campbell, Mutual inductances of circuits composed of straight wires, Phys. Rev. **5**, 452 (1915).

[37] F. Martens, Über die gegenseitige Induktion und ponderomotorische Kraft zwischen zwei stromdurchflossenen Rechtecken, Ann. Phys. **334**, 959 (1909).

[38] W. Sierpinski, Sur une courbe dont tout point est un point de ramification, Compt. Rend. Acad. Sci. Paris **160**, 302 (1915).

[39] S. Lepri, C. Trono, and G. Giacomelli, Complex Active Optical Networks as a New Laser Concept, Phys. Rev. Lett. **118**, 123901 (2017).

[40] M. Gaio, D. Saxena, J. Bertolotti, D. Pisignano, A. Camposeo, and R. Sapienza, A nanophotonic laser on a graph, Nat. Commun. **10**, 1 (2019).

[41] A. Lubatsch and R. Frank, A self-consistent quantum field theory for random lasing, Appl. Sci. **9**, 2477 (2019).

[42] L. M. Massaro, S. Gentilini, A. Portone, A. Camposeo, D. Pisignano, C. Conti, and N. Ghofraniha, Heterogeneous random laser with switching activity visualized by replica symmetry breaking maps, ACS Photon. **8**, 376 (2021).

[43] C. Forestiere, G. Miano, M. Pascale, and R. Tricarico, Electromagnetic scattering resonances of quasi-1-d nanoribbons, IEEE Trans. Antennas Propag. **67**, 5497 (2019).

[44] W. Eccles, Wireless telegraphy and telephony: A handbook of formulae, data and information, Nature **102**, 63 (1918).